

RE-CREATION OF AN APOLLO-ERA SEPARATION ANOMALY USING A LOW-G SLOSH MECHANICAL ANALOG

William J. Elke III*, Ryan J. Caverly†

The formulation of a dynamic model and simulation framework for a low-g slosh mechanical analog is first presented. Then, the simulation environment of an Apollo-era separation anomaly is thoroughly re-created, and a study of the anomaly that uses 1,260 simulations follows. The formulation, simulation, and study addresses the shortcomings of a publication from the Apollo era, which contains errors in its formulation, provides insufficient information to recreate results, and limits its analysis to ten simulations. The correct formulation and complete simulation environment provide a benchmark case to which different low-g slosh mechanical analogs can be compared. Results are presented, which show good agreement with the results from the Apollo-era publication and corroborates its conclusions.

INTRODUCTION

Recent interest in sending humans to the lunar and martian surfaces has led to spacecraft designs with large ratios of liquid propellant to dry mass [1]. Large amounts of liquid propellant can lead to significant coupling between the rigid-body dynamics of the spacecraft and the motion, or slosh, of the liquid within its propellant tank. These spacecraft-propellant interactions can degrade the performance of the vehicle; therefore, a thorough analysis of the impact of slosh is required. The interactions that take place in a low-g environment, which is characterized by small relative accelerations between the spacecraft and its propellants [2–4], are of particular interest since the study of low-g slosh is a complicated undertaking and remains an active area of research.

The model used in the analysis of the effects of low-g slosh should be simple enough to capture the fundamental physics required for the studying the problem, but no simpler. From a flight mechanics perspective, this means a model that can predict the forces and moments acting on the spacecraft and the motion of the bulk liquid that causes them. One common approach is to use computational fluid dynamics (CFD) solvers to determine the slosh forces and moments acting on the spacecraft in offline simulations, then apply them to the spacecraft in a separate guidance, navigation, and control (GNC) simulation. This approach is able to predict the forces, moments, and motion of

*Aerospace Engineer, Dynamic Systems and Control Branch, NASA Langley Research Center, 8 Langley Blvd., MS 308, Hampton, VA, 23681.

†Assistant Professor, Department of Aerospace Engineering and Mechanics, University of Minnesota, 110 Union St SE, Minneapolis, MN 55455.

the slosh with great fidelity, but such fidelity is not frequently required in the analysis of the flight mechanics. Drawbacks of this approach include the lack of coupling between the fluid and rigid-body dynamics, the harsh computational burden, and the complexities involved with tuning the CFD simulations [4].

The primary alternative to the CFD approach uses low-order approximate models of the liquid (sometimes called mechanical analog models), which aim to adequately capture the gross effects of the propellant slosh on the motion of the spacecraft. An added benefit of the mechanical models is they can run in real time. Such models have many space GNC applications; for example, (1) assessing degradation of handling qualities in the presence of low-g slosh dynamics during manual rendezvous proximity operations and docking events when there is a significant amount of propellant on board the spacecraft, (2) incorporating the model into an attitude navigation filter, and (3) assessing clearance margins and recontact probabilities during separation and jettison events.

There are many mechanical models, including second-order oscillators [2–5], particle models [6–10], and moving pulsating sphere models [11, 12]. Each of these models have different capabilities and use cases, which continue to mature. For the particle model, the liquid is modeled as a lumped mass translating within a containing boundary. The extent of the applicability of each of the mechanical models is an open research problem, but the particle model is well suited for low-g slosh problems involving large amplitude oscillation and gross liquid reorientation. The particle model is attractive for its simplicity, analytical tractability, heritage, and scalability. Furthermore, it is capable of capturing the complete general motion of the liquid.

Reference [8] is the first to use a particle model to analyze the effects of liquid slosh on the motion of a spacecraft in a low-g environment. It presents the derivation of the dynamics of a combined spacecraft-particle model and applies it to the study of an anomaly that occurred during the Apollo program. This anomaly involved the service module (SM) potentially colliding with the command module (CM) following separation prior to reentry, and is described in detail later in this paper. More than 50 years after its publication, [8] is still highly relevant and a great foundation for low-g slosh mechanical model research; however, it contains some errata as well as some missing information. The derivation of the dynamic model contains some errors, which are discussed in [10]. The analysis found in [8] mentions performing simulations of the trajectory of the SM with ten initial conditions, but not enough information about the initial conditions is presented to recreate the results. Of the ten simulations, [8] states that five “indicated the possibility of retrograde motion,” but provides no additional insight into that statement. Furthermore, results are presented for only one of the ten simulations.

The objectives of this paper are to develop a simulation framework of a rigid spacecraft with a single slosh particle, recreate the initial conditions of the CM/SM separation event by piecing together information from literature and historical data, then expand upon the analysis of the anomalous SM motion found in [8] by running the simulation with more initial conditions. The contributions re-

sulting from this are (1) the formulation of the particle model that addresses the errors found in [8], (2) the validation of this particle model with its original use case, and (3) the reconstruction of this Apollo-era-based test case that can be used as comparison for different low-g slosh models.

The particle model has many design choices and tuning parameters such as the friction model, effective mass fraction (the fraction of liquid contributing to the motion), constraint surface geometry, collision model, and adhesion force. The simulation used for this study is an extension of the work presented in [10], which is a particle model that is closely related to those found in [8, 9]. The differences between this model and the model found in [8] are that it (1) uses a single particle instead of two, (2) contains the particle within an ellipsoid instead of the tank geometry, (3) models the collision as instantaneous using the principles of impulse and momentum, (4) models friction as a linear viscous friction model instead of the empirical function presented therein, (5) considers an adhesion force between the tank wall and liquid, and (6) considers gravity. The primary difference between this model and the model found in [9] is that the collision is modeled as an instantaneous transfer of momentum instead of as a force that is a function of penetration depth and speed. Each of the features of the particle models can be tuned semi-analytically or with data from experiments or CFD simulations. The parameters and initial conditions chosen in this study are taken directly from [8] or the related NASA report [13] when available, computed from existing historical documents, or reasoned logically. For consistency, the units used throughout this paper are those used in [8, 13].

The remainder of the paper consists of four sections. The **LOW-G SLOSH MECHANICAL ANALOG** section presents the dynamic modeling and simulation of the particle model used in the analysis. In the section devoted to the **CASE STUDY**, the problem is described, the initial conditions of the CM/SM separation event are discussed, and then finally the particle model is employed to study the anomalous motion. Conclusions are presented in the final section.

LOW-G SLOSH MECHANICAL ANALOG

This section presents a description of the dynamic modeling and simulation framework of a spacecraft with a low-g slosh mechanical analog. First, the equations of motion for the system are given, in which case the system has nine degrees of freedom. This is followed by an approach to accommodate constrained motion that occurs when the particle is in contact with the constraint surface, in which case there are eight degrees of freedom. Finally, the collision dynamics are presented, which transition the system from unconstrained to constrained motion.

The SM is modeled as a spacecraft with low-g liquid slosh where the spacecraft bus is modeled as a rigid body, B , and the liquid propellant moving within a tank is approximated with the mechanical analog of a single particle, P , moving within a boundary known as a constraint surface [9]. This dynamic model of the SM is shown in Figure 1. Point b denotes the location of the center of mass of B , point p denotes the location of particle P , point c is fixed to B at the origin of the constraint

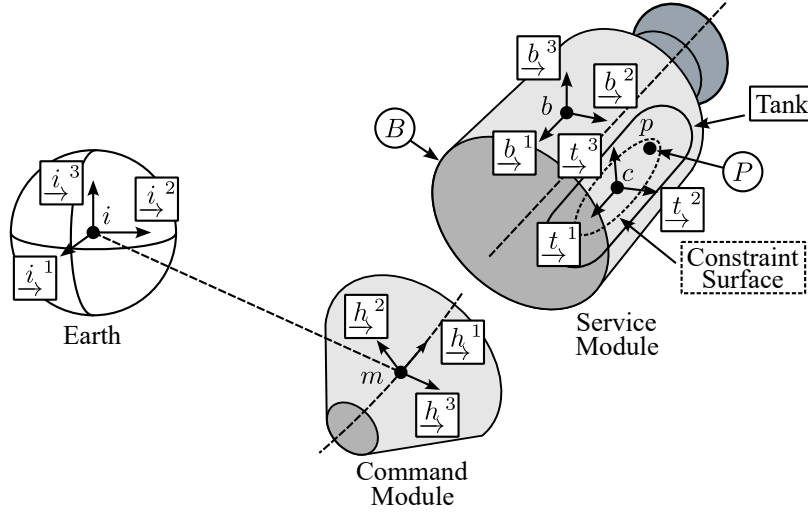


Figure 1: Definition of the frames and bodies of the dynamic system.

surface. \mathcal{F}_i is the Earth-centered inertial frame comprised of basis vectors \underline{i}^1 , \underline{i}^2 , and \underline{i}^3 . \mathcal{F}_b is a spacecraft-fixed reference frame comprised of basis vectors \underline{b}^1 , \underline{b}^2 , and \underline{b}^3 . For generality, \mathcal{F}_t is defined as a reference frame fixed to the constraint surface comprised of basis vectors \underline{t}^1 , \underline{t}^2 , and \underline{t}^3 since the orientation of the tank may not align with \mathcal{F}_b . The basis vectors for each frame are mutually orthonormal and dextral.

Some additional features are defined here for use in the **CASE STUDY** section. Hill's frame \mathcal{F}_h is used to describe the relative position and velocity of the SM relative to the CM. \mathcal{F}_h , which is comprised of basis vectors \underline{h}^1 , \underline{h}^2 , and \underline{h}^3 , is shown in Figure 1. \underline{h}^3 is the direction from the center of the orbit to the CM, \underline{h}^2 is in the direction of the angular momentum vector of the orbit, and \underline{h}^1 is given by the cross product $\underline{h}^2 \times \underline{h}^3$. Point m denotes the location of the center of mass of the CM.

The unconstrained equations of motion for the systems B and P are

$$m_B \dot{\mathbf{v}}_i^{bi/i} = \mathbf{f}_i^B, \quad (1)$$

$$\mathbf{J}_b^{Bb} \dot{\boldsymbol{\omega}}_b^{bi} + \boldsymbol{\omega}_b^{bi \times} \mathbf{J}_b^{Bb} \boldsymbol{\omega}_b^{bi} = \boldsymbol{\tau}_b^B, \quad (2)$$

$$m_P \dot{\mathbf{v}}_i^{pi/i} = \mathbf{f}_i^P, \quad (3)$$

where m_B is the mass of B , $\mathbf{v}_i^{bi/i}$ is the velocity vector of b relative to i in \mathcal{F}_i , \mathbf{f}_i^B is the result of the external forces acting on the spacecraft, \mathbf{J}_b^{Bb} is the second moment of mass of the spacecraft relative to b in \mathcal{F}_b , $\boldsymbol{\omega}_b^{bi}$ is the angular velocity of \mathcal{F}_b relative to \mathcal{F}_i , $\boldsymbol{\tau}_b^B$ is the resultant external torque acting on B , the dot in $\dot{\mathbf{x}}$ indicates a time derivative of \mathbf{x} , $(\cdot)^\times : \mathbb{R}^3 \rightarrow \mathbb{R}^{3 \times 3}$, is the cross operator that creates a three-by-three skew-symmetric matrix, which allows for cross products to be represented as matrix multiplication, m_P is the mass of P , $\mathbf{v}_i^{pi/i}$ is the velocity vector of p relative to i in \mathcal{F}_i ,

and \mathbf{f}_i^P is the result of the external forces acting on the particle. Equations (1), (2), and (3) can be expressed as

$$\underbrace{\begin{bmatrix} m_B \mathbf{1}_{3 \times 3} & \mathbf{0}_{3 \times 3} & \mathbf{0}_{3 \times 3} \\ \mathbf{0}_{3 \times 3} & \mathbf{J}_b^{Bb} & \mathbf{0}_{3 \times 3} \\ \mathbf{0}_{3 \times 3} & \mathbf{0}_{3 \times 3} & m_P \mathbf{1}_{3 \times 3} \end{bmatrix}}_{\mathbf{M}} \underbrace{\begin{bmatrix} \dot{\mathbf{v}}_i^{bi/i} \\ \dot{\boldsymbol{\omega}}_b^{bi} \\ \dot{\mathbf{v}}_i^{pi/i} \end{bmatrix}}_{\dot{\mathbf{v}}} = \underbrace{\begin{bmatrix} \mathbf{f}_i^B \\ \boldsymbol{\tau}_b^B \\ \mathbf{f}_i^P \end{bmatrix}}_{\mathbf{f}} + \underbrace{\begin{bmatrix} \mathbf{0}_{3 \times 3} \\ -\boldsymbol{\omega}_b^{bi \times} \mathbf{J}_b^{Bb} \boldsymbol{\omega}_b^{bi} \\ \mathbf{0}_{3 \times 3} \end{bmatrix}}_{\mathbf{f}}, \quad (4)$$

where $\mathbf{1}$ is the identity matrix and $\mathbf{0}$ is a matrix of zeros.

The contents of \mathbf{f}_i^B , $\boldsymbol{\tau}_b^B$, and \mathbf{f}_i^P considered here are gravity and the thrust from the reaction control system (RCS) thrusters. That is, $\mathbf{f}_i^B = \mathbf{f}_i^{g,B} + \mathbf{C}_{bi}^T \mathbf{f}_b^{\text{rcs}}$, $\boldsymbol{\tau}_b^B = \boldsymbol{\tau}_b^{\text{rcs}}$, and $\mathbf{f}_i^P = \mathbf{f}_i^{g,P}$, where \mathbf{C}_{bi} is the direction cosine matrix (DCM) representing the attitude of \mathcal{F}_b relative to \mathcal{F}_i . The gravity gradient torque is small relative to other torques acting on the body, therefore it is neglected. The gravity model used here is Newton's law of gravitation

$$\mathbf{f}_i^{g,B} = -\frac{\mu m_B}{|\mathbf{r}_i^{bi}|^3} \mathbf{r}_i^{bi}, \quad \mathbf{f}_i^{g,P} = -\frac{\mu m_P}{|\mathbf{r}_i^{pi}|^3} \mathbf{r}_i^{pi}, \quad (5)$$

where $\mu = 1.40785026 \times 10^{16} \text{ ft}^3/\text{s}^2$ is the gravitational constant of Earth, \mathbf{r}_i^{bi} is the position vector to b from i resolved in \mathcal{F}_i , \mathbf{r}_i^{pi} is the position vector to p from i resolved in \mathcal{F}_i , and $|\cdot|$ is the magnitude of (\cdot) . The values for the forces and moments resulting from the RCS thrusters are derived in the **CASE STUDY** section. The thrusters are on significantly longer than the period of the dynamics, therefore, the dynamics of the thrusters are neglected. The dynamics of the thruster actuators are neglected because the duration of the thruster firings considered here are orders of magnitude larger than the period of the dynamics.

Constraint and friction forces are added to Eq. (4) as

$$\mathbf{M}\dot{\mathbf{v}} = \mathbf{f} + \mathbf{f}^c + \mathbf{f}^f, \quad (6)$$

to account for the contact between the particle and constraint surface, where \mathbf{f}^c are the constraint forces and \mathbf{f}^f are the friction forces. The friction forces are based on the viscous friction model

$$\mathbf{f}^f = \begin{bmatrix} C_f \mathbf{v}_i^f \\ C_f \mathbf{r}_b^{pb \times} \mathbf{C}_{bi} \mathbf{v}_i^f \\ -C_f \mathbf{v}_i^f \end{bmatrix}, \quad (7)$$

where C_f is the coefficient of friction, \mathbf{r}_b^{pb} is the position vector to p from b resolved in \mathcal{F}_b , and \mathbf{v}_i^f is defined as the velocity of p relative to c in \mathcal{F}_i that is tangent to the constraint surface. The constraint

force \mathbf{f}^c in Eq. (6) is related to the Lagrange multipliers via

$$\mathbf{f}^c = (\mathbf{\Lambda}^\top(\mathbf{q}))_{(n \times m)} \boldsymbol{\lambda}_{(m \times 1)}, \quad (8)$$

where $\mathbf{\Lambda}(\mathbf{q})$ is the constraint matrix, $\mathbf{q} \triangleq \left[\mathbf{r}_i^{bi^\top} \quad \mathbf{q}_b^{bi^\top} \quad \mathbf{r}_i^{pi^\top} \right]^\top$, $\mathbf{q}_b^{bi} \in \mathbb{R}^{9 \times 1}$ is the stack of the elements of \mathbf{C}_{bi} , and $\boldsymbol{\lambda}$ are the Lagrange multipliers—in this case, $m = 1$ for one constraint. The constraint matrix is derived from the equation of the constraint surface.

The constraint surface considered here is an ellipsoid of revolution centered within the tank with an axis of symmetry aligned with the axis of symmetry of the tank. This geometry is selected because it can be expressed with a function that is simple and continuous, it can vary with fill level of the tank to restrict the range of motion of the particle, and approximates the constraint surface geometries found in [6, 7], which are derived empirically. The ellipsoid of revolution is used for the constraint surface in [9] with similar reasoning. The constraint equation for an ellipsoid of revolution is

$$\frac{x^2}{a_1^2} + \frac{y^2 + z^2}{a_2^2} = 1, \quad (9)$$

where (x, y, z) describes a location on the ellipsoid, a_1 is the length of the semi-axis along the axis of revolution, and a_2 is the length of the other semi-axes. The computation of a_1 and a_2 are functions of the tank geometry and fill level, and are described in detail in the **APPENDIX**. Equation (9) is the constraint equation, which can be expressed in terms of \mathbf{q} as

$$C(\mathbf{q}) = \underbrace{\mathbf{r}_t^{pc^\top} \begin{bmatrix} a_1^{-2} & 0 & 0 \\ 0 & a_2^{-2} & 0 \\ 0 & 0 & a_2^{-2} \end{bmatrix}}_{\mathbf{W}_t} \mathbf{r}_t^{pc} - 1 = 0, \quad (10)$$

where $\mathbf{r}_t^{pc} \triangleq \mathbf{r}_t^{pc}(\mathbf{q}) = -\mathbf{C}_{ti} \mathbf{r}_i^{bi} - \mathbf{C}_{tb} \mathbf{r}_b^{cb} + \mathbf{C}_{ti} \mathbf{r}_i^{pi}$, \mathbf{C}_{ti} is the DCM representing the attitude of \mathcal{F}_t relative to \mathcal{F}_i , \mathbf{C}_{tb} is the DCM representing the attitude of \mathcal{F}_t relative to \mathcal{F}_b , and \mathbf{r}_b^{cb} is the position vector to c from b resolved in \mathcal{F}_b . To obtain $\mathbf{\Lambda}$, $C(\mathbf{q})$ is differentiated with respect to time to determine the velocity level constraint

$$\dot{C}(\mathbf{q}, \boldsymbol{\nu}) = 2\mathbf{r}_t^{pc^\top} \mathbf{W}_t \dot{\mathbf{r}}_t^{pc} = 0, \quad (11)$$

where $\boldsymbol{\nu} \triangleq \left[\mathbf{v}_i^{bi/i^\top} \quad \boldsymbol{\omega}_b^{bi^\top} \quad \mathbf{v}_i^{pi/i^\top} \right]^\top$. Using the relationship

$$\dot{\mathbf{r}}_t^{pc} = -\mathbf{C}_{ti} \mathbf{v}_i^{bi/i} + \mathbf{C}_{tb} \mathbf{r}_b^{cb \times} \boldsymbol{\omega}_b^{bi} + \mathbf{r}_t^{pc \times} \mathbf{C}_{tb} \boldsymbol{\omega}_b^{bi} + \mathbf{C}_{ti} \mathbf{v}_i^{pi/i},$$

Eq. (11) can be rearranged into the form

$$\dot{C}(\mathbf{q}, \boldsymbol{\nu}) = \underbrace{\begin{bmatrix} -2\mathbf{r}_t^{pc\top} \mathbf{W}_t \mathbf{C}_{ti} & 2\mathbf{r}_t^{pc\top} \mathbf{W}_t (\mathbf{r}_t^{pc\times} \mathbf{C}_{tb} + \mathbf{C}_{tb} \mathbf{r}_b^{cb\times}) & 2\mathbf{r}_t^{pc\top} \mathbf{W}_t \mathbf{C}_{ti} \end{bmatrix}}_{\boldsymbol{\Lambda}} \boldsymbol{\nu} = 0. \quad (12)$$

The constraint forces in Eq. (8) can be obtained by using the acceleration level constraint. To get the acceleration level constraint, the time derivative of Eq. (12) is taken, which yields

$$\ddot{C}(\mathbf{q}, \boldsymbol{\nu}, \dot{\boldsymbol{\nu}}) = \boldsymbol{\Lambda} \dot{\boldsymbol{\nu}} + \dot{\boldsymbol{\Lambda}} \boldsymbol{\nu} = 0. \quad (13)$$

Equations (6), (8), and (13) are combined to be expressed as

$$\begin{bmatrix} \mathbf{M} & -\boldsymbol{\Lambda}^\top \\ -\boldsymbol{\Lambda} & \mathbf{0}_{m \times m} \end{bmatrix} \begin{bmatrix} \dot{\boldsymbol{\nu}} \\ \boldsymbol{\lambda} \end{bmatrix} = \begin{bmatrix} \mathbf{f} + \mathbf{f}^f \\ \dot{\boldsymbol{\Lambda}} \boldsymbol{\nu} \end{bmatrix}. \quad (14)$$

Equation (14) can be solved algebraically to find $\dot{\boldsymbol{\nu}}$ and $\boldsymbol{\lambda}$ as long as $\boldsymbol{\Lambda}$ is full rank and \mathbf{M} is invertible, which is true for the system at hand. First, $\boldsymbol{\lambda}$ is solved for via

$$\boldsymbol{\lambda} = -(\boldsymbol{\Lambda} \mathbf{M}^{-1} \boldsymbol{\Lambda}^\top)^{-1} (\dot{\boldsymbol{\Lambda}} \boldsymbol{\nu} + \boldsymbol{\Lambda} \mathbf{M}^{-1} (\mathbf{f} + \mathbf{f}^f)), \quad (15)$$

then $\dot{\boldsymbol{\nu}}$ follows from Eqs. (6) and (8).

An algebraic relation of $\boldsymbol{\nu}$ is applied at the transition from unconstrained (Eq. (4)) to constrained motion (Eq. (6)) to impose the constraint [14]. Reference [8] represents the imposition of the constraint with an inelastic collision model, which involves discontinuous fluid motion and instantaneous energy loss, but no further details are presented. Reference [10] derives this model mathematically using a coefficient of restitution, which is employed here. Let t_1 and t_2 be the time just before and after the collision, respectively. The total translational and angular momentum of the system through the collision are conserved, which are expressed as

$$m_B \mathbf{v}_i^{bi/i}(t_1) + m_P \mathbf{v}_i^{pi/i}(t_1) = m_B \mathbf{v}_i^{bi/i}(t_2) + m_P \mathbf{v}_i^{pi/i}(t_2), \quad (16)$$

$$\begin{aligned} m_B \mathbf{r}_b^{bs\times} \mathbf{C}_{bi} \mathbf{v}_i^{bi/i}(t_1) + \mathbf{J}_b^{Bb} \boldsymbol{\omega}_b^{bi}(t_1) + m_P \mathbf{r}_b^{ps\times} \mathbf{C}_{bi} \mathbf{v}_i^{pi/i}(t_1) \\ = m_B \mathbf{r}_b^{bs\times} \mathbf{C}_{bi} \mathbf{v}_i^{bi/i}(t_2) + \mathbf{J}_b^{Bb} \boldsymbol{\omega}_b^{bi}(t_2) + m_P \mathbf{r}_b^{ps\times} \mathbf{C}_{bi} \mathbf{v}_i^{pi/i}(t_2), \end{aligned} \quad (17)$$

where $\mathbf{r}_b^{bs} \triangleq -\frac{m_P}{m_B+m_P} \mathbf{r}_b^{pb}$ is the location of b relative to the center of mass of the total system at point s and $\mathbf{r}_b^{ps} \triangleq \frac{m_B}{m_B+m_P} \mathbf{r}_b^{pb}$ is the location of p relative to s . The collision model is expressed as

$$e = \frac{\mathbf{e}_i^{1\top} \mathbf{v}_i^{p'i/i}(t_2) - \mathbf{e}_i^{1\top} \mathbf{v}_i^{pi/i}(t_2)}{\mathbf{e}_i^{1\top} \mathbf{v}_i^{p'i/i}(t_1) - \mathbf{e}_i^{1\top} \mathbf{v}_i^{pi/i}(t_1)}, \quad (18)$$

where e is the coefficient of restitution, $\mathbf{v}_i^{p'i/i}$ is the velocity of spacecraft at the point of contact relative to i in \mathcal{F}_i , and \mathbf{e}_i^1 is the unit vector normal to the surface pointing outwards from the constraint surface in \mathcal{F}_i . For a perfectly inelastic collision $e = 0$, therefore Eq. (18) becomes

$$\mathbf{e}_i^{1\top} \mathbf{v}_i^{p'i/i}(t_2) - \mathbf{e}_i^{1\top} \mathbf{v}_i^{pi/i}(t_2) = 0. \quad (19)$$

Substituting relations $\mathbf{e}_i^1 = \mathbf{C}_{ti}^\top \mathbf{W}_t \mathbf{r}_t^{pc}$ and $\mathbf{v}_i^{p'i/i} = \mathbf{v}_i^{bi/i} + \mathbf{C}_{bi}^\top \mathbf{r}_b^{pb\times} \boldsymbol{\omega}_b^{bi}$ into this equation yields

$$(\mathbf{C}_{ti}^\top \mathbf{W}_t \mathbf{r}_t^{pc})^\top \mathbf{v}_i^{bi/i}(t_2) - (\mathbf{W}_t \mathbf{r}_t^{pc})^\top \mathbf{C}_{bi} \mathbf{r}_b^{pb\times} \boldsymbol{\omega}_b^{bi}(t_2) - (\mathbf{C}_{ti}^\top \mathbf{W}_t \mathbf{r}_t^{pc})^\top \mathbf{v}_i^{pi/i}(t_2) = 0. \quad (20)$$

Equation (20) describes the motion of the system only in the direction normal to the constraint surface. Assuming there is negligible friction in the collision, the velocity of the particle in the plane tangent to the collision is going to be the same at t_1 and t_2 . This relationship is expressed as

$$\mathbf{e}_i^{2\top} \mathbf{v}_i^{pi/i}(t_2) = \mathbf{e}_i^{2\top} \mathbf{v}_i^{pi/i}(t_1), \quad (21)$$

$$\mathbf{e}_i^{3\top} \mathbf{v}_i^{pi/i}(t_2) = \mathbf{e}_i^{3\top} \mathbf{v}_i^{pi/i}(t_1), \quad (22)$$

where \mathbf{e}_i^2 is the unit vector pointing in the direction of \mathbf{v}_i^f and \mathbf{e}_i^3 completes the cross product $\mathbf{e}_i^3 = \mathbf{e}_i^{1\times} \mathbf{e}_i^2$. Equations (16), (17), and (20)–(22) can be solved algebraically for $\boldsymbol{\nu}$ at t_2 .

When the particle separates from the wall, the transition from constrained to unconstrained motion is accomplished switching to Eq. (4) from Eq. (6). Separation occurs when the force pulling on the particle to keep it constrained to the surface exceeds a threshold. Let $\mathbf{f}^{c,P}$ be the components of \mathbf{f}^c corresponding to the constraint forces acting on the particle. The particle separates when $-\mathbf{e}_i^{1\top} \mathbf{f}^{c,P} > f_{adh}$, where f_{adh} is the adhesion force threshold.

CASE STUDY: REVISITING APOLLO-ERA REENTRY ANOMALIES

This section describes a relatively unknown anomaly that occurred during the reentry phase of NASA's Apollo missions 7–11 and the subsequent mitigation efforts. Observations made in [8] are recreated and investigated further through the use of the combined spacecraft and particle dynamics model presented in the previous section.

Problem Description

During the Apollo program, the command and service module (CSM) carried the crew and the Apollo lunar module to lunar orbit and then back to Earth. Prior to Earth reentry, the SM would separate from the CM to expose the thermal protection system of the CM. After separation, the SM should have either skipped out of the atmosphere or, if not, the debris of the SM that survived reentry should have landed in the ocean downrange of the CM. There was a discrepancy, however, between the pre-flight predictions and the post-flight best-estimated trajectories of the SM during

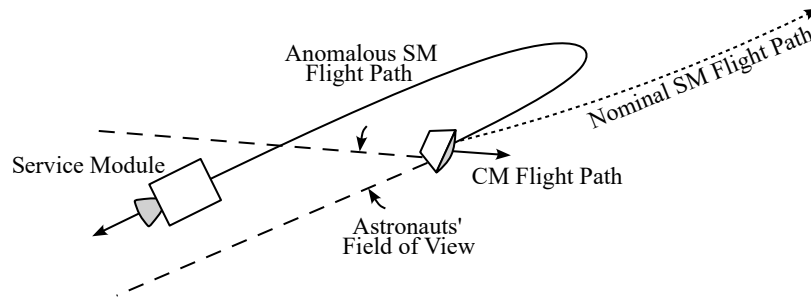


Figure 2: Depiction of the anomalous service module (SM) flight path relative to the command module (CM).

the missions of Apollo 7-11. Tracking data of the SM on these flights shows that the actual separation velocity of the SM was much smaller compared to pre-flight simulations [8, 13]. In fact, the separation velocity decreased such that the trajectory of the SM apparent to the CM was suggestive of a boomerang—it would first fly away, then return in the direction of the CM. This is supported by the observations of the Apollo 7 and Apollo 11 crews, who reported that they saw the SM through the window of the CM* [13]. The flight path of the SM would not have entered the astronauts’ field of view unless retrograde motion occurred. Figure 2 shows a depiction of the planned nominal trajectory and the estimated anomalous trajectory.

An internal investigation at the time concluded that this potentially catastrophic, unintended retrograde motion was primarily attributed to the gross reorientation of the residual propellant inside the tanks of the SM interacting with the preset reaction control system (RCS) thruster firing sequence, thus reducing the total separation velocity [13]. The now-publicly available technical memorandum [13] resulting from the internal investigation advises shortening the thruster on-times of the open-loop RCS thruster firing sequence to eliminate the retrograde motion. The revised firing sequence was first implemented on the SM of Apollo 13 and successfully used on all subsequent missions. Reference [8] uses a two-particle model to capture the interaction effects between the residual propellant inside the fuel and oxidizer tanks with spacecraft bus, and demonstrates the potential for this anomalous retrograde motion using the original RCS thruster firing sequence. Reference [13] uses a so-called “six-degree-of freedom” simulation but does not provide additional information regarding the model. Based on the timing of and similarities between the analyses presented in [8] and [13], it is suspected that similar or even the same modeling methodologies are used.

Reference [8] states that ten simulations of the SM separation event are performed for the analysis therein. The case study presented here augments this number by performing 1,260 simulations with two variations in the RCS thruster firing sequence, three values of particle masses, 35 values for particle initial positions, and six values for coefficient of friction. These values are described in the **Simulation Setup** section below.

*<https://apolloinrealtime.org/11/?t=194:54:41>

Simulation Setup

The preset RCS thruster firing sequences are stated clearly in [8, 13]. The timing and sequence of events are listed in Table 1. The firing sequence that resulted in the retrograde motion is referred to

Table 1: Sequence of events for the preset reaction control system (RCS) thruster firing sequences.

Time after separation (s)	Events	
	Original	Revised
0	-x jets on	-x jets on
2	+x roll jets on	+x roll jets on
4		+x roll jets off
7.5	+x roll jets off	
25		-x jets off
300	-x jets off	

as the original, and the firing sequence implemented to eliminate the retrograde motion is referred to as the revised. Reference [8] states that each thruster generates 100 lbf of thrust, and [13] states that four thrusters are used each for the $-x$ separation burn and the $+x$ roll spin-up. Note \mathcal{F}_b is defined to be aligned with the SM body-fixed reference frame xyz in [8, 13] as shown in Figure 1. Reference [8] also states that the center of mass of the SM lies off the centerline at $(y, z) = (-5.8, 10.9)$ in. This offset results in a moment being applied while the $-x$ jets are on, which necessitated the spin-up maneuver for spin stability. This information yields the RCS body forces and torques $\mathbf{f}_b^{\text{rcs}} = [-400 \ 0 \ 0]^T$ lbf and $\boldsymbol{\tau}_b^{\text{rcs}} = [0 \ 363.33 \ 193.33]^T$ ft-lbf when the $-x$ jets are on. Assuming the RCS jets are mounted at the SM circumference with a 12.8 ft diameter such that the force couples cancel, the resulting torque is calculated to be $\boldsymbol{\tau}_b^{\text{rcs}} = [2,560 \ 0 \ 0]^T$ ft-lbf when the four $+x$ roll jets are on.

Reference [8] states that the ten initial conditions used in the simulations varied in particle mass values and particle initial positions, but a limited set of values are provided. The single set of values for the masses of the oxidizer and fuel presented in [8] are 850 lbm and 370 lbm, respectively, for a total 1,220 lbm. Reference [13] supplements this with three additional values of the residual propellant masses. Figures 2–4 of [13] show the results of the three simulations with mass values of 1,100, 3,300, and 8,600 lbm. These values not only cover a wide range of fill ratios, but also cover the range of values of the residual propellant masses from the Apollo missions, which can be found in Table 1 of [13]. For consistency, this case study uses particle mass values $m_P = 1,220$ lbm, 3,300 lbm, and 8,600 lbm. The mass of the oxidizer and fuel are combined since the simulation framework used in this study assumes a single particle. The size of the constraint surface is adjusted to correspond to the different fill ratios and the results are shown in Table 2.

The initial position of the particle used in [8] can be gleaned from Figure 5 of that document. It

Table 2: Mass and semi-axes of the constraint surface for each fill ratio.

Parameter	Fill Ratio 1	Fill Ratio 2	Fill Ratio 3	Unit
m_P	1,220	3,300	8,600	lbm
a_1	5.79	5.15	3.72	ft
a_2	1.98	1.77	1.26	ft

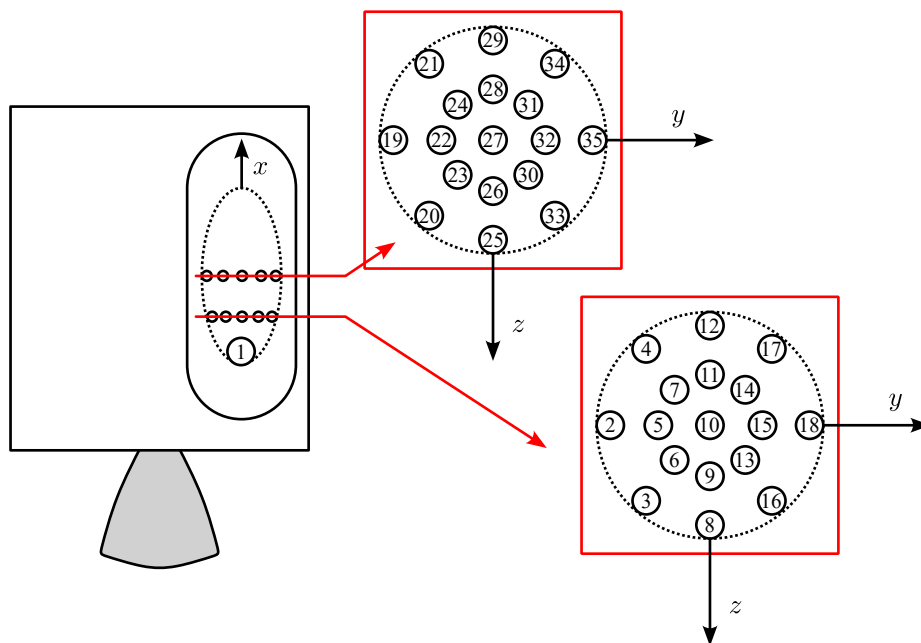


Figure 3: Dispersed particle initial positions used in the simulations.

appears the particle begins at the aft end of the tank. No information on the initial radial offset is available. The initial position of the particle used in [13] appears to be at the middle of the tanks from the results—again, no information about the radial offset from the centerline is shown. Knowledge of the mission can also inform initial particle position based on where the liquid propellant would be settled before separation. The Final Flight Evaluation Report for the Apollo 7 Mission [16] outlines the sequence of events and their timings. CM/SM separation took place 4 min, 17.5 s after the deorbit burn by the main engine. During this time, the propellant experienced small, surface tension-dominated motion. Therefore, the propellant was most likely settled somewhere between the middle and aft ends of the tanks just as [8, 13] appear to assume. Note this sequence of events took place on all Apollo missions with some variability in the timings so it is safe to assume the settled propellant configuration was the same for all missions. Based on these conclusions, this study uses the thirty-five different initial positions of the particle shown in Figure 3: one at the aft end of the constraint surface, seventeen spaced at the middle, and seventeen spaced at the plane halfway between the middle and aft end of the tanks.

Selecting the value of C_f is not straightforward since the friction model in [8] differs from the one used here. References [6,9] use the same friction model as used here, but the value of C_f is set to zero in [6] and is not discussed in depth in [9]. It is known that estimating the model for the viscous dissipative force in general is challenging. For this study, C_f is treated as an independent variable to account for the lack of accuracy in its value. Overall, the viscous dissipative force is small so C_f should also be small. A parametric study was first performed with $C_f = 0$ lbm/s, 400 lbm/s, 800 lbm/s, 1,200 lbm/s, 1,600 lbm/s, and 2,000 lbm/s to inform the final values to be used in this case study. It was concluded that a reasonable value of C_f lies between 100 lbm/s and 600 lbm/s. The resulting friction forces are on the same order of magnitude as seen in the model presented in [8]. Therefore, $C_f = 100$ lbm/s, 200 lbm/s, 300 lbm/s, 400 lbm/s, 500 lbm/s, and 600 lbm/s for the simulations presented in this case study.

The remaining simulation parameter values are used in all simulations. Since it is known that entry interface occurred about ten minutes after separation [16], the total simulation time is 600 s. Reference [8] gives the values of the mass properties of the SM as $m_B = 10,650$ lbm and

$$\mathbf{J}_b^{Bb} = \begin{bmatrix} 33.14 & -0.49 & 2.10 \\ -0.49 & 55.88 & -2.67 \\ 2.10 & -2.67 & 53.74 \end{bmatrix} \times 10^6 \text{ lbm-in.}^2,$$

which are assumed to be constant. The initial position and velocity of the SM are calculated using the ephemeris data from Apollo 7 found in [17]. The orbit described by the data is of the CSM just prior to the deorbit burn of the service propulsion system (SPS). The orbit after the burn is calculated by instantaneously reducing the the CSM's velocity in the \underline{h}_y^1 direction by the ΔV computed via

$$\Delta V = -\frac{T\Delta t}{m_f - m_0} \ln(m_f/m_0), \quad (23)$$

where $T = 21,500$ lbf is the thrust of the SPS, $\Delta t = 10$ s, $m_0 = 25,500$ lbm, and $m_f = 23,750$ lbm [13, 16]. For simplicity, it is assumed that the variations in residual propellant for the particle simulation did not affect m_0 or m_f . Though the burn lasts 10 s, it is assumed that the ΔV is applied impulsively since the duration of the burn is very small compared to the orbit. The initial position and velocity of the orbit just after the deorbit burn are then

$$\mathbf{r}_i^{bi} = \begin{bmatrix} 11.975 \\ 16.938 \\ 7.2007 \end{bmatrix} \times 10^6 \text{ ft}, \quad \mathbf{v}_i^{bi/i} = \begin{bmatrix} -20.949 \\ 10.110 \\ 9.1750 \end{bmatrix} \times 10^3 \text{ ft/s.}$$

It is assumed that the CSM is pointing the SPS exactly in the direction of its velocity $\mathbf{v}_i^{bi/i}$ at the

time of separation and that \underline{b}^3 is aligned with \underline{h}^3 . This corresponds to the initial DCM

$$\mathbf{C}_{bi} = \begin{bmatrix} 0.8245774112 & -0.423500770 & -0.375125565 \\ -0.150493778 & 0.474976738 & -0.867034441 \\ 0.545365670 & 0.771391079 & 0.327920858 \end{bmatrix}.$$

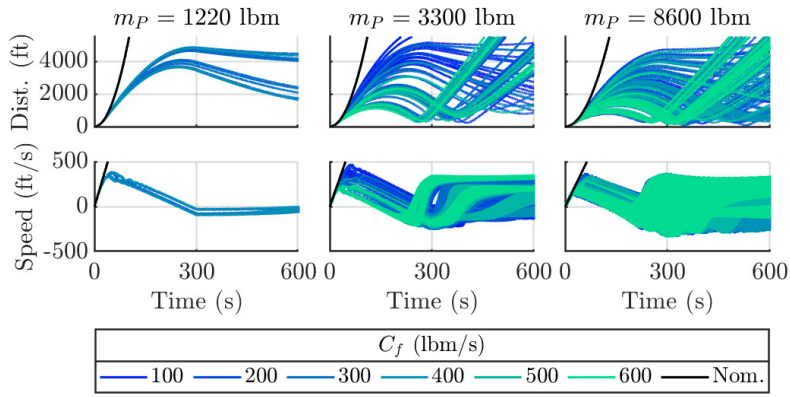
It is assumed that the initial angular velocity of the CSM is $\boldsymbol{\omega}_b^{bi} = \mathbf{0}_{3 \times 1}$. The constraint surface is located at $\mathbf{r}_b^{cb} = [0 \ 38.4 \ 0]^T$ in. with an orientation of $\mathbf{C}_{tb} = \mathbf{1}_{3 \times 3}$. This is close to the location of the oxidizer sump, which can be seen in Figure 2 of [8].

Results and Discussion

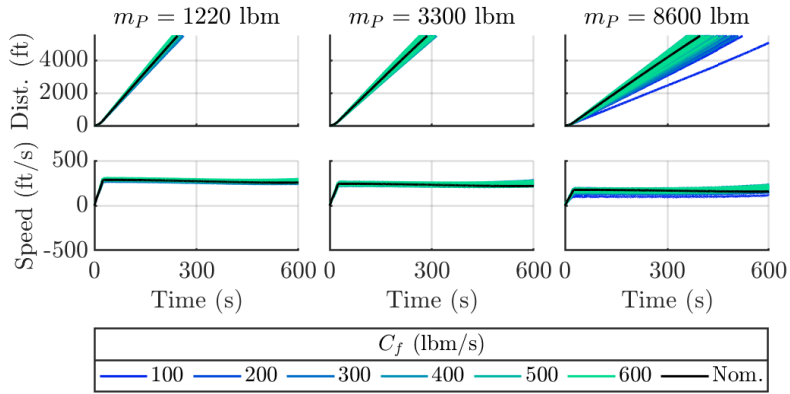
To perform an analysis of the trajectory of the SM with slosh, simulations of the CM and the rigid body SM without slosh are performed. The trajectory of the CM is simulated to obtain the relative position and velocity of the SM. The dynamics of the rigid body SM without the particle are simulated for each of the three particle mass values and preset RCS firing sequences. In these “nominal” six simulations, the corresponding propellant mass is added to m_B . In each of the figures presented below, the nominal simulations are plotted with a solid black line. For clarity, only the simulations using the original RCS firing sequence that exhibit retrograde motion are plotted in the figures below. As will be shown, the simulations using the revised RCS thruster firing sequences do not exhibit any retrograde motion; therefore, all of these simulations are plotted.

Figure 4 includes plots of the SM separation distance and speed versus time for both the original and revised RCS firing sequences (see Table 1). The separation distance is the total distance the SM is from the CM calculated by $|\mathbf{r}_i^{bm}|$. The separation speed is the velocity of the SM in the direction from the CM calculated by $\frac{\mathbf{r}_i^{bm \top}}{|\mathbf{r}_i^{bm}|} \mathbf{v}_i^{bm/i}$. Retrograde motion occurs when the value of the separation speed becomes negative. Figure 4a shows that retrograde motion occurs at each value of the particle mass m_P . Although retrograde motion does occur with $m_P = 1220$ lbm, it does not come close to the CM prior to entry interface. A trend observed in Figure 4a is that the number of cases that exhibit retrograde motion increases with m_P . It also shows that the distance of closest approach of the SM decreases as m_P increases. No contact occurs between the CM and SM in any of the simulations, but the SM gets as close as 60 ft in some cases. Figure 4b shows that the revised RCS firing sequence successfully eliminates all possibility of retrograde motion.

Figure 5 includes plots of the SM spin orientation versus time for the first 60 s of the simulation. Let $\theta(t)$ be defined as the angle between the longitudinal axis of the SM, x , at $t = 0$ and t as shown in Figure 5a. When $\cos \theta(t) = 1$, the SM is pointing in the same direction as it was at the time of separation. Conversely, when $\cos \theta(t) = -1$, the SM is pointing in the direction opposite to what it was at separation. Therefore, when the $-x$ jets are on and $\cos \theta(t) < 0$, there is some component of thrust pointing backwards resulting in a decrease in the separation velocity. Figure 5b shows



(a) Results from the simulations that use the original RCS firing sequence.



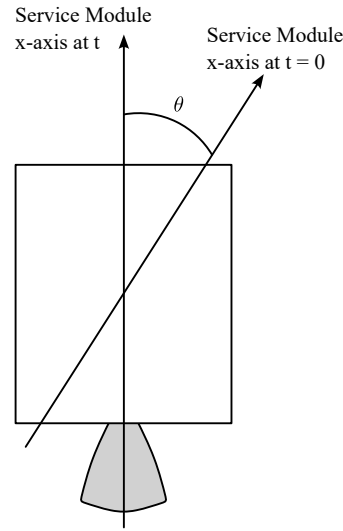
(b) Results from the simulations that use the revised RCS firing sequence.

Figure 4: Plot of the service module’s (SM) separation distance and speed versus time.

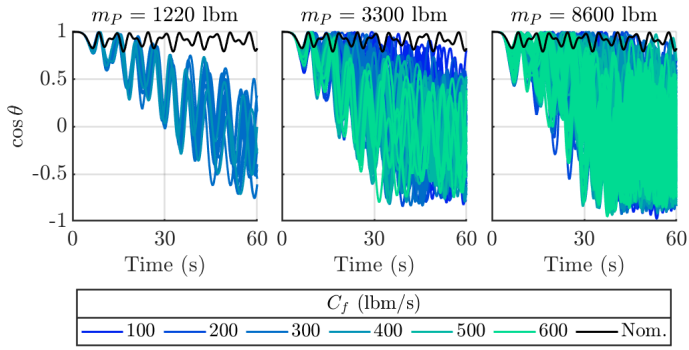
$\cos \theta$ becomes negative within the first 60 s after separation in all cases that produce retrograde motion—some as fast as 24 s. This corroborates the assessment of [13] that the RCS thrusters reduce the separation velocity of the SM, and the root cause is the interaction between the original RCS thruster firing sequence and the perturbed angular motion of the SM due to slosh. Figure 5c shows that, in all cases of the revised RCS firing sequence, $\cos \theta$ does not become negative before $t = 25$ s, which is when the $-x$ RCS jet firings stop.

Figure 6 includes plots of the longitudinal location of the particle within the constraint surface, x , versus time for the simulations using the original RCS firing sequence. Figure 6 shows the particle gets pushed to the front end of the tank and stays there as the spacecraft transitions to a major axis rotation. It is also apparent that, in general, the time it takes for the particle to settle decreases as C_f increases. This is likely a result of the increased energy damping from increased friction. There does not appear to be any strong correlation between the mass of the particle and the overall settling time. Figure 6 is in good agreement with Figure 5 of [8] and Figures 2–4 of [13].

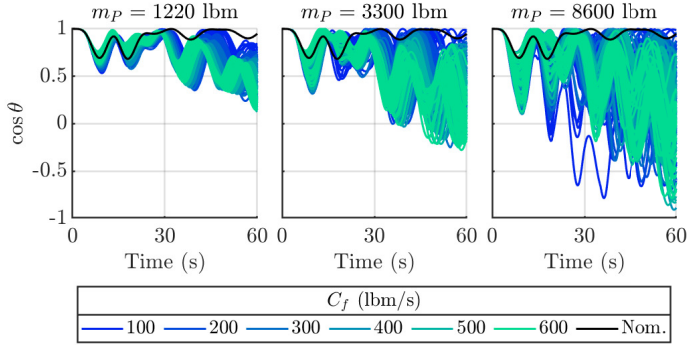
Figure 7 includes plots of the SM trajectory relative to the CM resolved in Hill’s frame from the



(a) Definition of $\theta(t)$, the angle between the x-axis of the SM at $t = 0$ and t .



(b) Results from the simulations that use the original RCS firing sequence.



(c) Results from the simulations that use the revised RCS firing sequence.

Figure 5: Definition of $\theta(t)$ and plots of the service module's (SM) spin orientation versus time.

simulations using the original RCS firing sequence. For the purposes of discussion, let \underline{h}^1 , \underline{h}^2 , and \underline{h}^3 directions be considered forward, left, and up relative to the CM, respectively, since the CM is traveling in the \underline{h}^1 direction and Earth is always in the $-\underline{h}^3$ direction. The trajectories from the nominal simulations show the SM fly forward, slightly left, and slightly up from the CM. The left and up motion is caused by offset between the center of mass and centerline of the SM. Recall that the original RCS firing sequence has the $-x$ jets fire for 2 s before the roll jets begin firing to give the vehicle spin stability, and that the SM is initially pointing directly backwards. In that time, the SM begins to point right and down so it travels left and up when the $-x$ jets fire. When it is spin-stabilized, it effectively maintains its pointing direction. When the particle motion is considered in the simulation, this initial pointing perturbation remains; however, it is additionally perturbed by the particle repositioning to the forward end of the constraint surface, as shown in Figure 6. The resulting collision and constraint forces impart a moment about the center of mass of the SM, pointing it slightly left and more down relative to the nominal case. This phenomenon can be seen between the plots of the three different masses. As m_P increases, the momentum transfer increases, causing the SM to point further left and down, which results in the SM traveling further up and

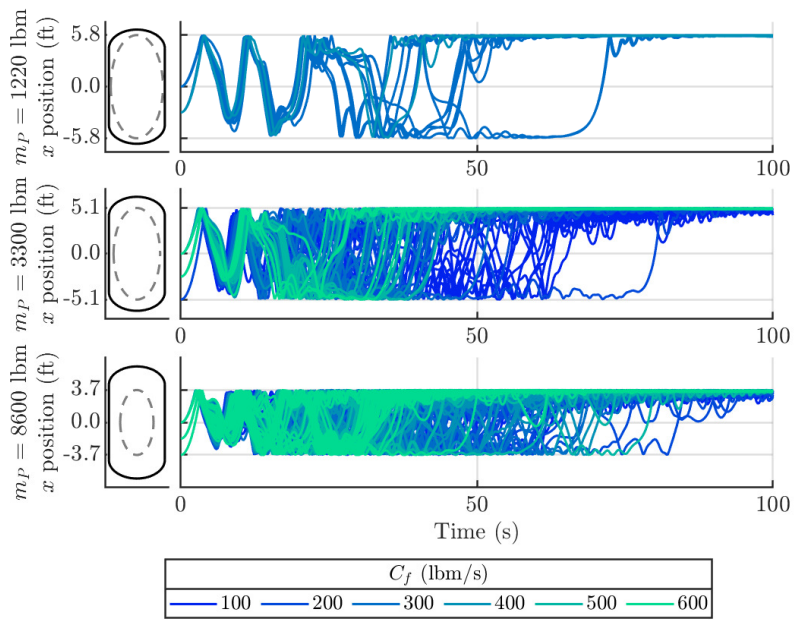


Figure 6: Plots of the x position of the particle within the constraint surface versus time for the original RCS thruster firing sequence.

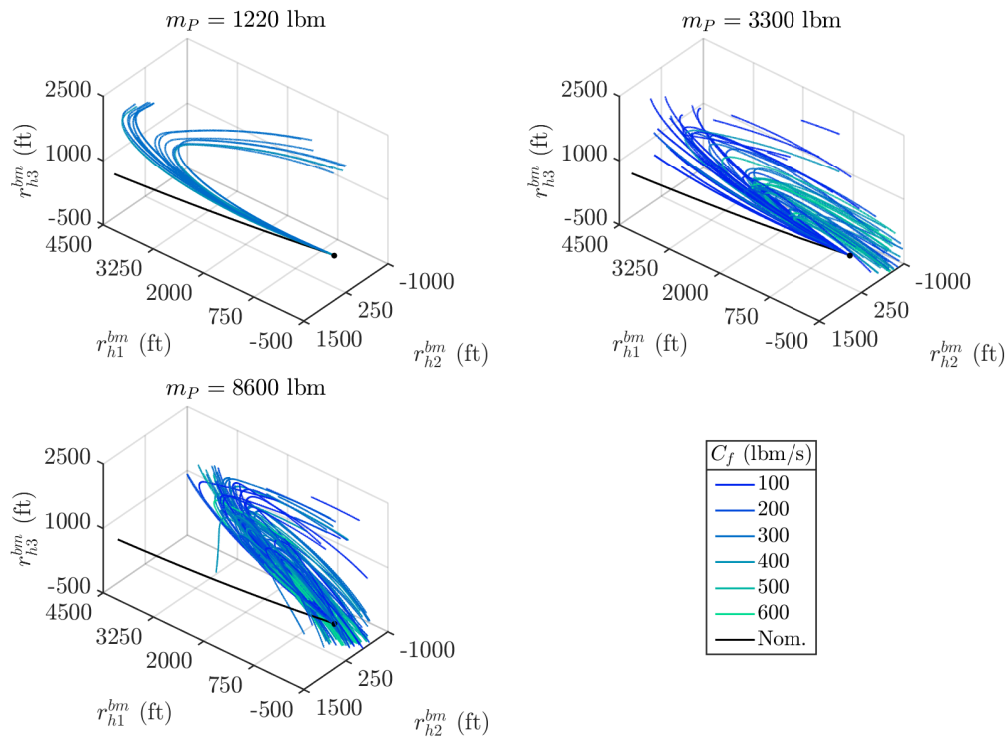


Figure 7: Plots of the service module's (SM) trajectory relative to the command module (CM) for the original RCS thruster firing sequence.

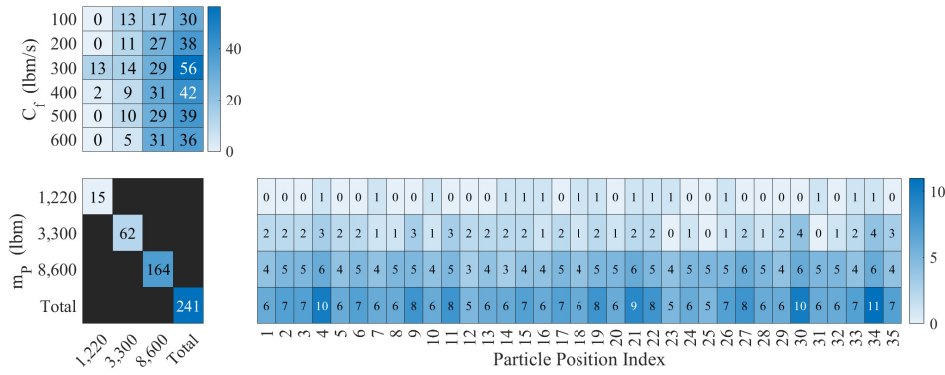


Figure 8: Number of simulations exhibiting retrograde motion as a function of independent variable out of the 630 simulations using the original RCS firing sequence. None of the simulations using the revised RCS firing sequence exhibited retrograde motion.

right relative to the nominal case. The SM then effectively maintains this pointing direction during the spin stabilization. Following the spin-up maneuver, the SM transitions to a major axis rotation from the motion of the particle and ensuing damping, allowing for some component of the RCS thrusters to point back in the direction of the CM, which decreases the separation velocity and causes retrograde motion. As m_P increases, the number of cases that exhibit retrograde motion increases. Also, the closest approach distance of the SM decreases, which is consistent with Figure 4a. This is due to the increased momentum transfer due to the increased mass of the particle. Figure 7 is in good agreement with Figure 9 of [8].

Figure 8 shows the correlation between each independent variable and propensity for retrograde motion. A total of three different particle masses, thirty-five initial positions of the particle, and six coefficients of friction are simulated. The darker the fill color of the box, the more simulations there are that exhibited retrograde motion for that case, with the number of cases listed in the box. For particle initial position (lower right plot), there is no correlation between particle initial position and the propensity for retrograde motion. For the coefficient of friction (upper left plot), there appears to be a Gaussian distribution as a function of C_f , with a peak at $C_f = 300$ lbm/s. As a conjecture, these observed trends can be explained by the fact that at lower friction values there is insufficient damping to cause the vehicle to fully transition from a minor axis to major axis spin, whereas at higher values of friction the particle slows down so much initially that damping becomes negligible thereafter. What is most obvious from Figure 8, however, is that the mass of the particle m_P has the greatest influence on whether the spacecraft will exhibit retrograde motion (lower left plot). A total of 241 out of the 630 simulations that used the original RCS thruster firing sequence exhibited retrograde motion. It is realistic to assume that [8] only considered values of the particle masses equivalent to the measured values of the residual propellant on the Apollo missions 7–11 in their analysis. These values are found in Table 1 of [13], which shows that the mass of residual propellant is well-represented by the values $m_P = 3,300$ lbm and $m_P = 8,600$ lbm. The total

number of simulations exhibiting retrograde motion for these two values is 226 out of 420 (53.8%). The probabilistic occurrence of retrograde motion predicted by this single tank model by varying the particle mass and initial particle location appear to match the ratio 5 out of 10 provided in [8].

The agreement between the results presented in this section and the results from [8, 13] suggest that the updated formulation of the particle model and the recreated simulation environment of the SM/CM separation event are valid, allowing them to be used to fill in the gaps from [8, 13].

CONCLUSION

This paper presented the development of a dynamic model and simulation framework that involves an approximate mechanical model of liquid propellant slosh within a spacecraft in a low-g environment, inspired by a model from the Apollo era. The propellant was modeled as a particle within an ellipsoidal constraint surface. The model was then simulated to analyze the anomalous trajectory of the Apollo-era service module after separation from the command module and prior to reentry. Reference [8] performed the same analysis using just ten simulations and concluded that 50% of the simulations “exhibited the possibility of retrograde motion.” Results from the study presented here corroborated that number as 53.8% of 420 simulations exhibit retrograde motion.

ACKNOWLEDGMENT

This material is based upon work supported by the Human Landing System (HLS) project under the Artemis program of NASA. This version of the contribution has been accepted for publication, after peer review (when applicable) but is not the Version of Record and does not reflect post-acceptance improvements, or any corrections. The Version of Record is available online at: [http://dx.doi.org/\[insertDOI\]](http://dx.doi.org/[insertDOI]). Use of this Accepted Version is subject to the publisher’s Accepted Manuscript terms of use <https://www.springernature.com/gp/open-research/policies/accepted-manuscript-terms>.

APPENDIX: CONSTRAINT SURFACE SIZING

Semi-axes a_1 and a_2 are functions of fill ratio, defined as the ratio of liquid volume to the empty volume of the tank. For a particular fill ratio, these parameters are computed as the distance from the centroid of the liquid to the center of the ellipsoid when the tank is stood on end or laid flat in a 1-g environment as shown in Figure 9. It is assumed that the contact angle at the liquid-gas interface is 90° . The ellipsoid of revolution is an approximation made to simplify the geometry of the constraint surface and is also used in [9]. The ellipsoid of revolution approximation may get worse as the fill ratio approaches zero or one, or if the tank is not a cylinder with hemispherical end caps. Two main advantages of this model are it (a) requires only two parameters to define the constraint surface, (b) is agnostic of tank geometry and fill level [6, 7].

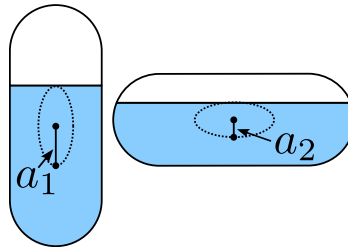


Figure 9: Semi-axes a_1 and a_2 of the constraint surface.

REFERENCES

- [1] E. Musk, “Making Humans a Multi-Planetary Species,” *New Space*, Vol. 5, June 2017, pp. 46–61, <https://doi.org/10.1089/space.2017.29009.emu>.
- [2] H. N. Abramson, “The Dynamic Behavior of Liquids in Moving Containers,” NASA SP-106, 1966.
- [3] F. T. Dodge, “The New Dynamic Behavior of Liquids in Moving Containers,” Southwest Research Institute, San Antonio, TX, 2000.
- [4] P. J. Enright and E. C. Wong, “Propellant Slosh Models for the Cassini Spacecraft,” *Astrodynamics Conference*, AIAA-94-3730-CP, Scottsdale, AZ, August 1994, pp. 186–195, <https://doi.org/10.2514/6.1994-3730>.
- [5] J. W. Jang, A. Alaniz, L. Yang, J. Powers, and C. Hall, “Mechanical Slosh Models for Rocket-Propelled Spacecraft,” *AIAA Guidance, Navigation, and Control (GNC) Conference*, AIAA 2013-4651, August 2013, <https://doi.org/10.2514/6.2013-4651>.
- [6] R. L. Berry and J. R. Tegar, “Experimental Study of Transient Liquid Motion in Orbiting Spacecraft,” NASA CR-144003, February 1975.
- [7] P. G. Good, A. Carpenter, H. Flanders, and T. Gardner, “STARDUST TCM and Despin in the Presence of Complex Fuel Dynamics,” *Advances in the Astronautical Sciences*, Vol. 99, AAS 98-142, February 1998, pp. 611–628.
- [8] D. H. Merchant, R. M. Gates, and J. F. Murray, “Prediction of Apollo Service Module Motion after Jettison,” *Journal of Spacecraft and Rockets*, Vol. 8, June 1971, pp. 587–592, <https://doi.org/10.2514/3.59697>.
- [9] Z. Zhou and H. Huang, “Constraint Surface Model for Large Amplitude Sloshing of the Spacecraft with Multiple Tanks,” *Acta Astronautica*, Vol. 111, February 2015, pp. 222–229, <https://doi.org/10.1016/j.actaastro.2015.02.023>.
- [10] W. J. Elke III, J. Pei, C. M. Roithmayr, and R. J. Caverly, “Framework for Analyzing the Complex Interactions Between Spacecraft Motion and Slosh Dynamics in Low-G Environments,” *73rd International Astronautical Congress*, IAC-22-C1.IPB.34.x72589, Paris, France, September 2022. Available: <https://ntrs.nasa.gov/citations/20220013204>.
- [11] J. P. B. Vreeburg, “Dynamics and Control of a Spacecraft with a Moving Pulsating Ball in a Spherical Cavity,” *Acta Astronautica*, Vol. 40, No. 2, 1997, pp. 257–274, [https://doi.org/10.1016/S0094-5765\(97\)00095-7](https://doi.org/10.1016/S0094-5765(97)00095-7).
- [12] M. Deng and B. Yue, “Nonlinear Model and Attitude Dynamics of Flexible Spacecraft with Large Amplitude Slosh,” *Acta Astronautica*, Vol. 133, 2017, pp. 111–120, <https://doi.org/10.1016/j.actaastro.2017.01.003>.
- [13] “Apollo 11 Mission Anomaly Report No. 3, Service Module Entry,” NASA MSC-03466, November 1970.
- [14] S. Djerassi, “Imposition of Constraints,” *Journal of Applied Mechanics*, Vol. 61, June 1994, pp. 434–439, <https://doi.org/10.1115/1.2901463>.

- [15] R. E. Kincade, "Summary of SM Entry for Apollo Missions 7, 8, 9, 10, and 11," NASA 69-FM37-323, August 1969.
- [16] "Final Flight Evaluation Report, Apollo 7 Mission," NASA TMX-64324, February 1969.
- [17] M. Grandfield, D. Hanlon, K. Hebb, E. Jentsch, R. Yorke, and M. R. Wolf, "Tracking Studies of Apollo 7 and Intelsat II," Smithsonian Astrophysical Observatory Special Report No. 298, April 1969.